

ORBITAL EVOLUTION OF MOONS IN WEAKLY ACCRETING CIRCUMPLANETARY DISKS

YURI I. FUJII¹, HIROSHI KOBAYASHI², SANEMICHI Z. TAKAHASHI³, OLIVER GRESSEL¹

¹ Niels Bohr International Academy, The Niels Bohr Institute, Blegdamsvej 17, DK-2100, Copenhagen Ø, Denmark

² Department of Physics, Nagoya University, Furo-cho, Showa-ku, Nagoya, Aichi, 464-8602

³ Astronomical Institute, Tohoku University, 6-3 Aramaki, Aoba-ku, Sendai, Japan, 980-8578

Draft version April 27, 2018

ABSTRACT

We investigate the formation of hot and massive circumplanetary disks (CPDs) and the orbital evolution of satellites formed in these disks. Because of the comparatively small size-scale of the sub-disk, quick magnetic diffusion prevents the magnetorotational instability (MRI) from being well-developed at ionization levels that would allow MRI in the parent protoplanetary disk. In the absence of significant angular momentum transport, continuous mass supply from the parental protoplanetary disk leads to the formation of a massive CPD. We have developed an evolutionary model for this scenario and have estimated the orbital evolution of satellites within the disk. We find, in a certain temperature range, that inward migration of a satellite can be stopped by a change in the structure due to the opacity transitions. Moreover, by capturing second and third migrating satellites in mean motion resonances, a compact system in Laplace resonance can be formed in our disk models.

Subject headings: planets and satellites: formation – planets and satellites: gaseous planets – proto-planetary disks

1. INTRODUCTION

Regular satellites around gas-giant planets are thought to form in a surrounding gaseous disk. This notion is supported by the near-circular orbits of the moon systems in our own Solar System, which are well-aligned to their equatorial-planes, except for irregular satellites that have been captured dynamically.

In analogy with a minimum mass solar nebula (Hayashi 1981) for planet formation, minimum mass sub-nebula models were introduced for satellite formation (e.g. Lunine & Stevenson 1982). For explaining certain characteristics of the Galilean moons, Canup & Ward (2002, 2006) introduced the so-called *gas-starved* disk model and reproduced the ratio between the planet mass and the total mass of the satellite system. Satellite formation around gas giants in a *solids-enhanced* minimum mass model was discussed by Mosqueira & Estrada (2003a,b) and Estrada & Mosqueira (2006) moreover developed a scenario in *gas-poor* environment. Sasaki et al. (2010) introduced an inner cavity in a gas-starved disk and found that several moons in a resonance can be formed. Based on this work, Ogihara & Ida (2012) performed N-body simulations and have shown that moons are commonly captured in a 2:1 mean motion resonance outside the cavity and Galilean-like configuration can be formed.

In contrast to the *nebula* hypothesis, relatively small rocky satellites present today can be well explained by a formation scenario in a tidal spreading disk (Charnoz et al. 2010; Crida & Charnoz 2012; Hyodo et al. 2015). The model is compelling, but it requires a disk of solid material as the starting point. Such circumplanetary “*debris*” disks may originate from the capture of planetesimals (e.g. Hyodo et al. 2016, 2017) or from tidal disruption of a previous generation of satellites. However, larger satellites, especially those that maintain an atmosphere, need gas around them during their accretion. Therefore, it is reasonable to assume that

at least some of the regular satellite systems must have originated from gaseous circumplanetary disks (CPDs).

When a protoplanet grows to the size of several earth masses in a protoplanetary disk (PPD) comparable to the one typically assumed for the early solar nebula (Hayashi 1981), gas around the planet starts to accrete onto it. At that time, because of the conservation of angular momentum, a rotationally supported disk forms around the planet. On theoretical grounds, CPDs can be observed in many hydrodynamic and magnetohydrodynamic (MHD) simulations (e.g. Tanigawa & Watanabe 2002; Klahr & Kley 2006; Ayliffe & Bate 2009; Machida et al. 2010; Szulágyi et al. 2014, 2017; Gressel et al. 2013; Perez et al. 2015). Because of the orders of magnitude difference in spatial scales, however, resolving the very vicinity of the planet in those simulations is still difficult. Tanigawa et al. (2012) have successfully measured the mass infall rate onto a CPD during the early stage of its evolution, but the long-term evolution remains to be established. Yet, the modeling a CPD fully self-consistently during the full PPD and planetary gap evolution is difficult just like modeling the formation of PPDs from cloud-collapse is difficult.

In PPDs, the magnetorotational instability (MRI) is thought to play an important role in facilitating the accretion of the disk gas. Although angular momentum transfer in a CPD was previously expected to be as effective as that in a PPD, sustaining the MRI is more difficult in CPDs (Fujii et al. 2011, 2014; Turner et al. 2014; Keith & Wardle 2014). Thermal ionization can trigger MRI at the inner radii of a CPD if the temperature becomes sufficiently high (Keith & Wardle 2014). However, in the absence of strong MRI turbulence, gas accretion may not be efficient enough to prevent a CPD from becoming massive by accumulation of infalling material. An alternative scenario for angular-momentum transport within the CPD may be provided by a magnetocentrifugal disk wind which has been found to operate sporadi-

cally in resistive-MHD simulations (Gressel et al. 2013). It remains to be shown whether CPD winds are equally emerging when including additional micro-physics such as ambipolar diffusion. In any case, disk outflows are generally competing with infall, and it is unclear how a steady state can be reached for CPDs that are still deeply embedded in their parent disks.

If the sub-disk grows so massive as to become gravitationally unstable, spiral arms appear and transfer angular momentum. Whether or not the gravitational energy is converted into heat *in situ* is still under debate, but supposed the energy deposition is local, the temperature with the CPD can become high. In such a situation, episodic accretion caused by a combination of the gravitational instability (GI) and the MRI (boosted by thermal ionization) is to be expected. Martin & Lubow (2011, 2013) and Lubow & Martin (2012, 2013) studied this phenomenon in a layered CPD model that is developed in the context of PPDs (e.g. Armitage et al. 2001).

As mentioned earlier, a CPD is likely to become massive in the absence of significant transport of angular momentum, that is if the temperature is insufficient to maintain MRI turbulence. In this paper, we develop an alternative model of the satellite-forming region of CPDs considering the mass inflow from the PPD as the dominant factor. Because there still is a gap between the spatial scales that can be well-resolved by full-blown 3D MHD simulations and the actual satellite-forming region (inside a few tens of planet radii), we pursue the strategy of 1D modeling of the sub-disk by means of an effective description based on results from numerical simulations.

By doing so, in some of our models, we find a bump in the radial surface density structure. We will examine whether such a specific location can stop the migration of moons. Given the situation that the innermost moon survives rapid inward type-I migration by convergent migration to the pressure maximum, we investigate the possibility of trapping the second and third moons in a mean motion resonance (MMR). The inner three of the Galilean moons are known to be in a 4:2:1 mean motion resonance, a so-called Laplace resonance. In some of our models, we successfully obtained a system in Laplace resonance.

This paper is organized as follows. In Section 2, we describe our sub-disk model and assumptions and resulting disks are shown in 3. We then highlight several models with interesting structure and discuss the orbital evolution of moons in the disks in Section 4. Discussion of the obtained results and a brief summary are given in Sections 5 & 6, respectively.

2. MODELING OF CIRCUMPLANETARY DISKS

2.1. Derivation of Surface Density and Temperature

The equation for the time evolution of surface density is essentially derived in the same way as in Fujii et al. (2014), but in addition, here we simultaneously solve for the *temperature* structure of the embedded sub-disk.

We determine the surface-density profile of the CPD by solving a diffusion equation with an additional source term stemming from mass infall from the parent PPD. When the sub-disk's angular velocity is taken to be Ke-

plerian, the evolution of the surface density is given by

$$\frac{\partial \Sigma}{\partial t} = \frac{1}{r} \frac{\partial}{\partial r} \left[3r^{1/2} \frac{\partial}{\partial r} \left(r^{1/2} \nu \Sigma \right) \right] + f, \quad (1)$$

where r is the radius, ν is the kinematic viscosity coefficient, and f is the mass flux from infall onto the CPD. We employ the standard α prescription of Shakura & Sunyaev (1973), namely, $\nu = \alpha c_s^2 / \Omega_K$ with c_s being the sound speed and Ω_K the Keplerian rotation frequency.

To determine a prescription for the source term f , we adopted the results of a detailed analysis of the 3D high-resolution simulations by Tanigawa et al. (2012). Even though they employed 11 levels of nested grids, the resolution is insufficient to resolve the vertical structure of the CPD in the innermost several Jupiter radii from the planet. Therefore, Tanigawa et al. measured physical values of infalling material at high altitude, where the infall is supersonic – the idea being that the infall rate obtained in this way is not affected by the uncertainty caused by the architecture of the CPD further downstream. The effective mass flux onto an inner part of CPD is $f(r) \propto r^{-1}$ (see Figure 15 of Tanigawa et al. 2012). We assume that the planet has $0.4 M_J$ and lies 5.2 AU away from a solar mass star. Based on the values at this distance in the minimum mass solar nebula (Hayashi 1981), the local surface density and sound velocity of the PPD are $\varepsilon \times 143 \text{ g cm}^{-2}$ and $4.58 \times 10^4 \text{ cm s}^{-1}$, respectively, where ε is a scaling factor representing the reduction of the surface density due to gas dissipation. With these values, we obtain the mass infall rate as

$$f = \begin{cases} 1.3 \times 10^{-3} \varepsilon \left(\frac{r}{R_J} \right)^{-1} \text{ g cm}^{-2} \text{ s}^{-1} & (r \leq 20R_J) \\ 0 & (r > 20R_J), \end{cases} \quad (2)$$

where R_J is one Jupiter radius. As the power-law index of the mass infall rate drops outside ~ 0.04 Hill radii from the planet (Tanigawa et al. 2012), we set $f = 0$ at $r > 20R_J$. The initial value $\varepsilon = 1$ corresponds to the beginning of the mass infall and a smaller value indicates a smaller mass infall rate. Since the viscous timescale of the CPD is sufficiently smaller than that of the PPD, we treat ε as a constant here.

We adopt the following simplified form used in previous studies (Cannizzo 1993; Armitage et al. 2001) to estimate the temperature structure, that is

$$\frac{\partial T_c}{\partial t} = \frac{2(Q_+ - Q_-)}{c_p \Sigma} - v_r \frac{\partial T_c}{\partial r}, \quad (3)$$

where $Q_+ = (9/8)\nu\Sigma\Omega_K^2$ represents the viscous heating, $Q_- = \sigma(1 + 3/8\kappa\Sigma)T_c^4$ is the radiative cooling, σ is the Stefan-Boltzmann constant, and v_r is the radial velocity. Further to this, the opacity κ is given by Bell & Lin (1994), summarized in Table 1 (see also table 1 of Kimura & Tsuribe 2012) as

$$\kappa = \kappa_0 \rho^a T^b, \quad (4)$$

where ρ is the density and T is the temperature. The specific heat is given by $c_p \simeq 2.7 \mathcal{R} / \bar{\mu}$, where \mathcal{R} is the ideal gas constant and $\bar{\mu} = 2.34$ is the mean molecular weight.

opacity regime	κ_0 ($\text{cm}^2 \text{g}^{-1}$)	a	b	Temperature range	
				from (K)	to (K)
Ices	2×10^{-4}	0	2	0	166.8
Sublimation of ices	2×10^{16}	0	-7	166.8	202.6
Dust	1×10^{-1}	0	1/2	202.6	$2286.7\rho^{2/49}$
Sublimation of dust	2×10^{81}	1	-24	$2286.7\rho^{2/49}$	$2029.7\rho^{1/81}$
Molecules	1×10^{-8}	2/3	3	$2029.7\rho^{1/81}$	$10000.0\rho^{1/21}$

Table 1
Bell and Lin opacity from Table 1 of Kimura & Tsuribe (2012)

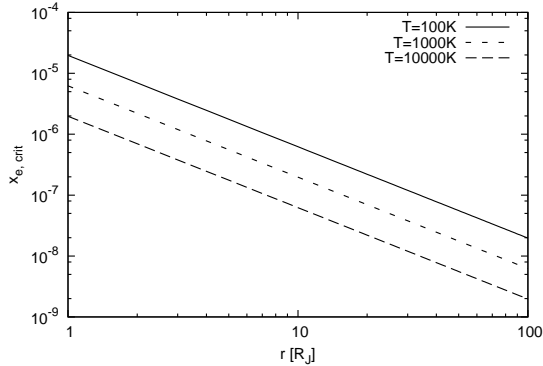


Figure 1. Critical ionization degree needed to sustain the MRI at the midplane at $T = 100$ K, 1000 K, and 10,000 K for $\beta_0 = 10^5$.

We solve Eqns. (1) and (3) numerically with boundary conditions of zero torque and vanishing temperature gradient at the inner and outer boundaries. The temperature of the PPD at the location of the sub-disk is assumed to be $T = 123$ K. We set the temperature of the CPD to this value whenever the calculated temperature is lower than this.

2.2. Origin of Viscosity

In this section, we explain how to obtain an estimate for the kinematic viscosity coefficient. The best-known origin of effective viscosity in accretion disks is via MRI turbulence. There are two criteria for the MRI that must be fulfilled for the instability to be active: the disk gas must be ionized enough to be coupled with magnetic field, and the magnetic field is not too strong (Balbus & Hawley 1991; Sano & Miyama 1999; Okuzumi & Ormel 2013). We consider the MRI if the following two conditions are satisfied:

1. the Elsasser number, $\Lambda \equiv v_{Az}^2/\eta\Omega_K > 1$, with $v_{Az} \equiv |B_z|/\sqrt{4\pi\rho}$ being the vertical component of the Alfvén velocity, and where η is the magnetic diffusivity, and
2. the z component of plasma beta defined in terms of net magnetic flux, $\beta_z = 2c_s^2/v_{Az}^2 \gtrsim 2000$; see Okuzumi & Ormel (2013) and Fujii et al. (2014) for details.

As suggested by the results of Fujii et al. (2011, 2014), Turner et al. (2014), and Keith & Wardle (2014), sub-disks are not likely to widely sustain well-developed MRI turbulence in the absence of thermal ionization.

If the disk is not subject to sustaining MRI turbulence, material may pile up and the disk eventually becomes gravitationally unstable. Accordingly, if the Toomre parameter,

$$Q \equiv \frac{\Omega_K c_s}{\pi G \Sigma}, \quad (5)$$

(with G the gravitational constant) becomes smaller than a value of 2, we employ an effective viscosity of $\alpha_{\text{GI}} \equiv \exp(Q^{-4})$ (Zhu et al. 2010; Takahashi et al. 2013). In such a case, the disk can be easily heated up provided that gravitational energy is converted into heat. It is widely assumed that thermal ionization can trigger the MRI if the temperature exceeds about 1000 K; however, in CPDs this is not always the case. First of all, the ionization fraction obtained from the Saha equation depends on density and a gravitationally unstable disk naturally has a high surface density. Secondly, for a CPD to sustain the MRI, the required ionization fraction is comparatively higher than that of a PPD even if the density is the same.

As is mentioned in Fujii et al. (2014), this is because typical length scale is orders of magnitude smaller in a sub-disk. Thus, the critical temperature is higher than 1000 K. If we adopt $\eta = 234(T/1\text{K})^{1/2} x_e^{-1} \text{cm}^2\text{s}^{-1}$ where $x_e \equiv n_e/n_n$ is ionization degree and n_e and n_n are respectively number density of electron and neutral gas (Blaes & Balbus 1994), the condition for sufficient ionization to sustain the MRI at midplane can be given as

$$\Lambda = \frac{2c_s^2 x_e}{234\sqrt{T/1\text{K}}\Omega_K\beta_0} > 1, \quad (6)$$

where β_0 is the plasma beta at the midplane. From this equation, we can derive the critical ionization degree needed to be MRI-active as $x_{e,\text{crit}} = 234\sqrt{T/1\text{K}}\Omega_K\beta_0/(2c_s^2)$.

As an illustration of this, Fig. 1 shows the critical ionization degree needed to have the MRI at the midplane for a disk with $\beta_0 = 10^5$. The plot is made for the disk temperatures of 100 K, 1000 K, and 10,000 K, respectively. Note that, with the “gas-starved” case of surface density as the lower limit, $\Sigma = 100 (r/20R_J)^{-3/4} \text{g cm}^{-2}$ (Canup & Ward 2002; Sasaki et al. 2010), midplane ionization degree at $10 R_J$, when $T = 1000$ K is assumed is only about 10^{-12} . One can easily see from Fig. 1 that this value is far below the critical value, x_{crit} , at the respective radius. The temperature needed to obtain $x_e > x_{e,\text{crit}}$ for this case is about 2000 K. Obviously, if the surface density is larger, higher temperature is required.

In this paper, we consider the thermal ionization of potassium, sodium, and magnesium. In the high-temperature regime, where most of the metals are already ionized, atomic hydrogen also becomes a dominant source of free electrons. At such temperatures, hydrogen gas is already dissociated, so we employ the following Saha equation for atomic hydrogen as well as for metals

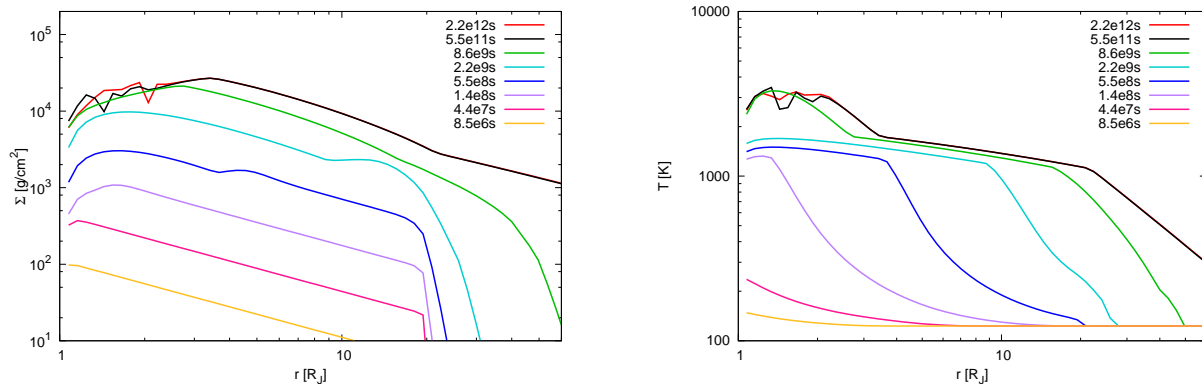


Figure 2. Time evolution of surface density (left) and temperature structure (right) for the case with $\varepsilon = 10^{-2}$ and $\alpha_{\text{floor}} = 10^{-4}$. Each color shows the different time of the evolution. The uppermost line in each plot shows the steady-state value except within $2.2 R_J$.

to solve for the ionization degree from collisions¹:

$$\frac{x_e x_{K^+}}{x_K} = \frac{2}{n_n} \left(\frac{2\pi m_e k_B T_c}{h^2} \right)^{3/2} \times \exp(-5.0 \times 10^4 / T_c) \quad (7)$$

$$\frac{x_e x_{Na^+}}{x_{Na}} = \frac{2}{n_n} \left(\frac{2\pi m_e k_B T_c}{h^2} \right)^{3/2} \times \exp(-6.0 \times 10^4 / T_c) \quad (8)$$

$$\frac{x_e x_{Mg^+}}{x_{Mg}} = \frac{2}{n_n} \left(\frac{2\pi m_e k_B T_c}{h^2} \right)^{3/2} \times \exp(-8.9 \times 10^4 / T_c) \quad (9)$$

$$\frac{x_e x_{H^+}}{x_H} = \frac{2}{n_n} \left(\frac{2\pi m_e k_B T_c}{h^2} \right)^{3/2} \times \exp(-1.6 \times 10^5 / T_c) \quad (10)$$

where, x_K etc. represent the number densities of each species, and m_e , h , and k_B are respectively electron mass, the Planck constant, and the Boltzmann constant. With those equations and charge neutrality, we finally obtain the ionization degree as

$$x_e = \left(\frac{2}{n_n} \right)^{1/2} \left(\frac{2\pi m_e k_B T_c}{h^2} \right)^{3/4} \times \left[\begin{aligned} &x_K \exp\left(\frac{-5.0 \times 10^4}{T_c}\right) \\ &+ x_{Na} \exp\left(\frac{-6.0 \times 10^4}{T_c}\right) \\ &+ x_{Mg} \exp\left(\frac{-8.9 \times 10^4}{T_c}\right) \\ &+ x_H \exp\left(\frac{-1.6 \times 10^5}{T_c}\right) \end{aligned} \right]^{1/2}. \quad (11)$$

We adopt Solar abundance multiplied by depletion factor δ for metal species, $x_K = 9.87 \times 10^{-8} \delta$, $x_{Na} = 1.60 \times 10^{-6} \delta$, and $x_{Mg} = 3.67 \times 10^{-5} \delta$, in our calculation.

¹ These expressions are approximately correct when the ionization fraction of each species is small, which is not appropriate for K and Na in this case. Since their abundance is small, however, the resulting ionization degree is not strongly affected.

If $\Lambda > 1$ is satisfied at the midplane, we set the viscous parameter due to the MRI turbulence as $\alpha_{\text{MRI}} = 1040/\beta_0 + 0.015$ (Okuzumi & Hirose 2011). Thus, we denote the Elsasser number at the midplane as Λ here after. What if the ionization degree is not high enough to sustain the MRI and the surface density is smaller than the critical value to be gravitationally unstable? There is always molecular viscosity, but it is negligibly small. Gravitational interaction between the star, planet and gas of a CPD can be an origin of angular momentum transport (Rivier et al. 2012). Kelvin-Helmholtz-like instabilities between sedimenting dust layers and gas can generate turbulence which can be roughly estimated as $\sim 10^{-4} - 10^{-3}$. Moreover, it has been found that in disks with imposed radial temperature gradients, the resulting vertical shear can be a robust source of turbulence via an analog of the Goldreich-Schubert-Fricke instability (Nelson et al. 2013). Rigorously establishing the presence of the vertical-shear instability in CPDs will, however, require us to derive constraints on radiative cooling timescales τ_{crit} similar to the work by Lin & Youdin (2015), who (in the context of PPDs) find the corresponding criterion to scale with the disk thickness – which is favorably large for the comparatively puffed-up CPDs, implying less-restrictive conditions on τ_{crit} .

There may be other ways of transporting angular momentum, however, those mechanisms contain uncertainties and the specific value is not yet obtained. Thus, we treat them via setting a floor value, α_{floor} , in this work. In summary, we define the viscous parameter as

$$\alpha = \alpha_{\text{MRI}} + \alpha_{\text{GI}} + \alpha_{\text{floor}} \quad (12)$$

$$\alpha_{\text{MRI}} = \begin{cases} \frac{1040}{\beta_0} + 0.015 & (\text{if } \Lambda > 1) \\ 0 & (\text{if } \Lambda \leq 1) \end{cases} \quad (13)$$

$$\alpha_{\text{GI}} = \begin{cases} \exp(Q^{-4}) & (\text{if } Q < 2) \\ 0 & (\text{if } Q \geq 2) \end{cases} \quad (14)$$

We take ε and α_{floor} as parameters and obtain structures of CPDs based on Section 2.1 above.

3. RESULTING DISK STRUCTURE

Since the timescale for ε to drop is uncertain, we simply develop a disk for each parameter set from scratch until it reaches a quasi-stationary state. First, we calculate assuming only 1% of metals are in gas phase, i.e.

$\delta = 0.01$. Figure 2 is an example of the formation of a CPD with $\varepsilon = 10^{-2}$ and $\alpha_{\text{floor}} = 10^{-4}$. Both surface density and temperature increase with time. The uppermost lines in Figure 2 show the values in the steady state except for within $\sim 2R_J$, where the radial profiles of the surface density and temperature remain non-steady and wiggle about.

In Fig. 3, the opacity, Elsasser number, Λ , and Q value at the final ε stage in Fig. 2 are shown. In the quiescent outer disk, the Elsasser number and Q parameter remain in the stable regime, that is $\Lambda < 1$ and $Q > 2$, and accordingly α is determined by α_{floor} . The Elsasser number occasionally exceeds unity in the inner disk and that prevents the system from settling into a stationary solution. Even if the inner disk remains time-variable, the outer disk achieves a steady state independent of the inner region. In the quiescent outer disk, a bump in the surface-density profile forms because of the increase of opacity due to the transition of the origin from dust sublimation to molecules. The dips in surface density (and temperature) at the inner domain border are related to the boundary conditions. Thus, we do not consider them as a bump.

Figure 4 shows the surface density profiles (left column) and temperature (right column) of various disk models once the outer disk has reached a steady state. One can see that models with larger ε and/or smaller α_{floor} generally become more massive and hotter. The top panels of Fig. 4 show the surface density and temperature structure for $\varepsilon = 10^{-1}$. Because the ionization degree reaches a near-critical value at the inner disk radii, the gas accretion rate fluctuates in time (illustrated by the shaded area in Fig. 4), and the disk structure is not fully stationary in this regime. When MRI enabled by thermal ionization is developed, depending on the settings, the disk either ends up with a steady state with smaller surface density or enters the gravito-magneto limit cycle studied by Lubow & Martin (2012, 2013).

The middle panels of Fig. 4 show the disk structure for $\varepsilon = 10^{-2}$. For the case of $\alpha_{\text{floor}} = 10^{-3}$ (green dotted line), relatively effective gas accretion keeps the surface density smaller than the cases for $\alpha_{\text{floor}} = 10^{-4}$ (blue solid line) and $\alpha_{\text{floor}} = 10^{-5}$ (pink dashed line). Since the temperature does not become high enough with $\alpha_{\text{floor}} = 10^{-3}$, the MRI is not triggered by thermal ionization and the whole disk settles into a steady state. Compared to the top panels, values are generally slightly smaller.

The bottom panel of Fig. 4 illustrates a case where the reduction factor decreases down to 10^{-3} . Because the infall flux is already small enough, the surface density does not become that massive, and therefore the temperature cannot be as high as supplying sufficient ionization to sustain the MRI. We remark that the surface-density range of our models is similar to the extended outer disk of Mosqueira & Estrada (2003a), but temperature is much higher in our models. For some parameter sets, a bump can be seen in surface density that is formed due to the change in opacity. A radial pressure bump cannot be seen in a disk with small ε and/or large α_{floor} because the surface density does not pile-up sufficiently for the inner disk to transition into the higher temperature regime required for the opacity transition.

Next, for the case when the temperature at which the

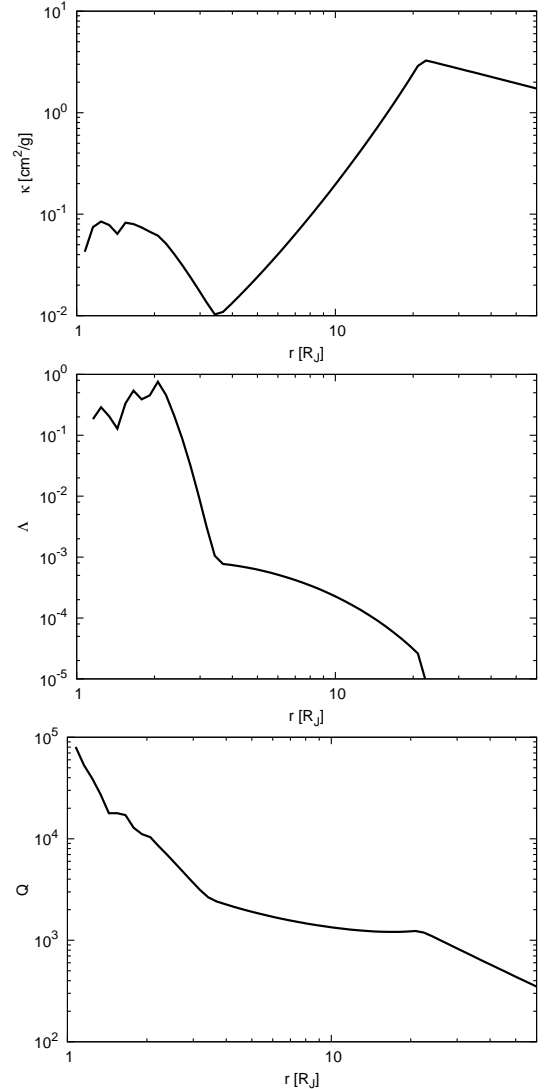


Figure 3. Radial profiles of opacity (top), Elsasser number (middle), and Toomre’s Q parameter (bottom panel) for the fiducial case with $\varepsilon = 10^{-2}$ and $\alpha_{\text{floor}} = 10^{-4}$.

thermal ionization plays a role for gas accretion is as high as the one for grains to evaporate, we calculate disk structures with $\delta = 1$ corresponding to solar abundance. We show the respective results in Fig. 5. For models with $\varepsilon = 10^{-3}$ (not show in the figure), we obtained identical profiles as in the case with $\delta = 0.01$ for all values of α_{floor} . This is also true for the model with $\varepsilon = 10^{-2}$ and $\alpha_{\text{floor}} = 10^{-3}$. For all other models, the range in which we do not obtain steady-state solutions slightly increase because thermal ionization can provide more electrons at the same temperature.

We conclude that the transition of the opacity regime from sublimation of dust to molecules can produce interesting structures in embedded CPDs for a variety of reasonable disk models. In the following section, we discuss the orbital evolution of (proto-)satellites in the disk models derived here.

4. CAPTURE OF SATELLITES IN RESONANT ORBITS

In the context of protoplanetary disks, disk-planet interaction has been studied extensively in the literature.

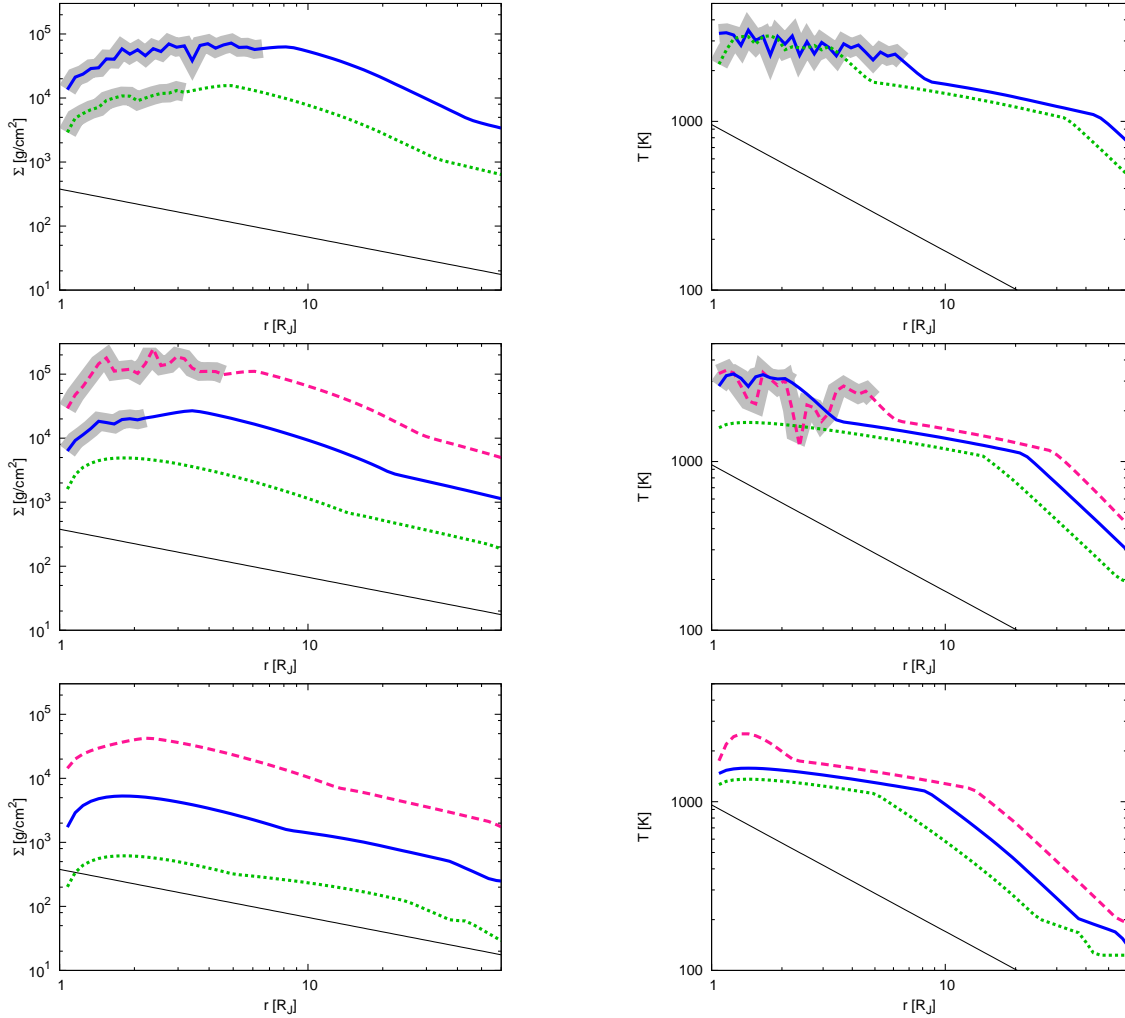


Figure 4. Steady-state surface density (left) and temperature (right) for $\varepsilon = 10^{-1}$, 10^{-2} , and 10^{-3} (from top to bottom) with $\delta = 0.01$ and various α_{floor} : dashed (pink), thick-solid (blue), dotted (green) lines show the case for $\alpha_{\text{floor}} = 10^{-5}$, 10^{-4} , and 10^{-3} , respectively. Shaded regions are not time-steady and display jitter. As a reference, a typical *gas-starved* disk profile is also plotted (solid black line).

Planets are believed to migrate in the hosting disk by exchanging their angular momentum with the disk. The idea is also introduced in satellite formation (for instance in Canup & Ward 2002, 2006; Sasaki et al. 2010; Ogihara & Ida 2012). As for PPDs, the migration direction and speed depend on the satellite mass and the disk structure, and the timescale is given as

$$t_m = \frac{1}{|b|} \left(\frac{M_s}{M_p} \right)^{-1} \left(\frac{\Sigma r^2}{M_p} \right)^{-1} \left(\frac{c_s}{v_K} \right)^2 \Omega_K^{-1}, \quad (15)$$

where M_s and M_p are the mass of the satellite and planet, respectively, and b is a constant that determines the direction and speed of the migration (Paardekooper et al. 2011; Kretke & Lin 2012; Ogihara et al. 2015). In this work, we only consider moons with circular orbits, and we use the formula of Paardekooper et al. (2011)² for the

migration constant b (see also Ogihara et al. 2015):

$$\begin{aligned} b = \frac{2}{\gamma} \{ & -2.5 - 1.7q + 0.1p \\ & + 1.1F(P_\nu)G(P_\nu) \left(\frac{3}{2} - p \right) \\ & + 0.7(1 - K(P_\nu)) \left(\frac{3}{2} - p \right) \\ & + 7.9 \frac{q - (\gamma - 1)p}{\gamma} F(P_\nu)F(P_\chi) \sqrt{G(P_\nu)G(P_\chi)} \\ & + \left(2.2 - \frac{1.4}{\gamma} \right) [q - (\gamma - 1)p] \\ & \times \sqrt{(1 - K(P_\nu))(1 - K(P_\chi))} \}, \quad (16) \end{aligned}$$

where γ is the adiabatic constant, $p \equiv -d \ln \Sigma / d \ln r$, and $q \equiv -d \ln T / d \ln r$. The expressions for $F(P)$, $G(P)$, and $K(P)$ are furthermore given as

$$F(P) = \left(1 + \left(\frac{P}{1.3} \right)^2 \right)^{-1} \quad (17)$$

² In their formula, which is derived as a fit to a set of simulations with a single perturbing body, the resulting torque from the entire disk is considered. For systems of multiple embedded bodies, the formula remains valid as long as all masses remain low enough, such that non-linear wake interaction can be ignored.

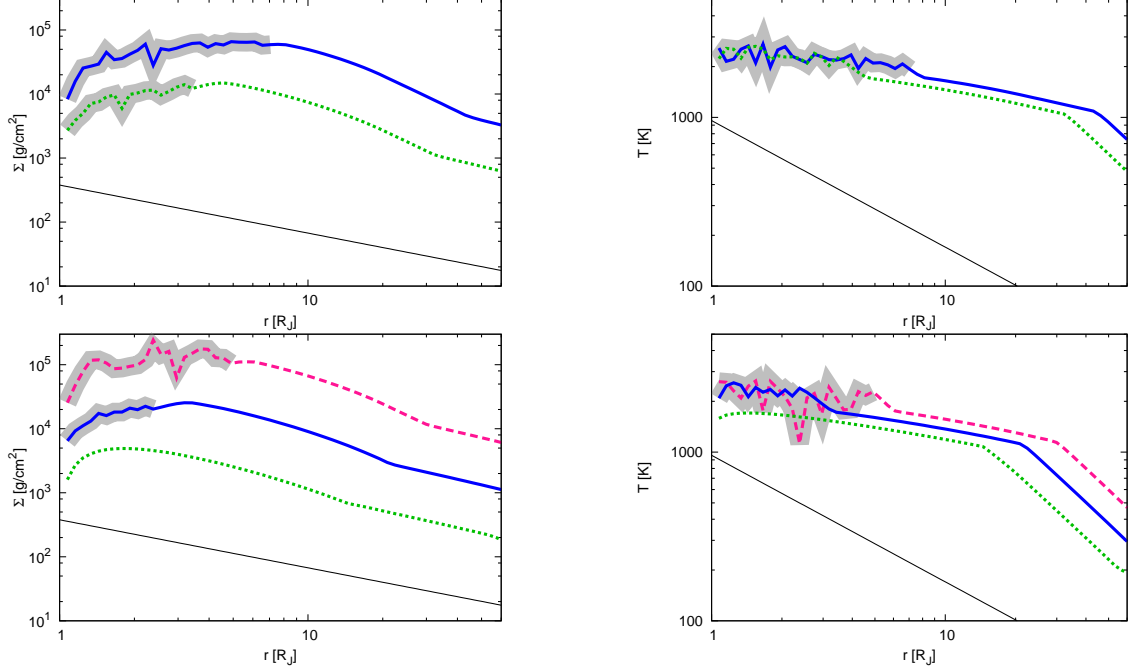


Figure 5. Same as Fig. 4 but for $\delta = 1$, that is, undepleted composition. The top panels are for $\varepsilon = 10^{-1}$ and the bottom panels are for $\varepsilon = 10^{-2}$. The results for $\varepsilon = 10^{-3}$ are not shown because they are identical to Figure 4.

	ε	α_{floor}
Models 1 & 1'	10^{-1}	10^{-4}
Models 2 & 2'	10^{-1}	10^{-3}
Models 3 & 3'	10^{-2}	10^{-5}
Models 4 & 4'	10^{-2}	10^{-4}
Models 5 & 5'	10^{-3}	10^{-5}

Table 2

Model parameters for the cases considered for orbital migration

$$G(P) = \begin{cases} \frac{16}{25} \left(\frac{45\pi}{8}\right)^{3/4} P^{3/2} & P < \sqrt{\frac{8}{45\pi}} \\ 1 - \frac{9}{25} \left(\frac{8}{45\pi}\right)^{4/3} P^{-8/3} & P \geq \sqrt{\frac{8}{45\pi}} \end{cases} \quad (18)$$

$$K(P) = \begin{cases} \frac{16}{25} \left(\frac{45\pi}{28}\right)^{3/4} P^{3/2} & P < \sqrt{\frac{28}{45\pi}} \\ 1 - \frac{9}{25} \left(\frac{28}{45\pi}\right)^{4/3} P^{-8/3} & P \geq \sqrt{\frac{28}{45\pi}} \end{cases} \quad (19)$$

We assume $\gamma = 1.4$ and that the thermal diffusivity is the same as ν (i.e., $\text{Pr}=1$). Thus, with the dimensionless half-width of the horseshoe region, $\chi_s = 1.1/\gamma^{1/4} \sqrt{M_s r / M_p h}$ (where h is the scale-height of the disk),

$$P_\nu = \frac{2}{3} \sqrt{\frac{\Omega_K \gamma^2 \chi_s^3}{2\pi\nu}} = \frac{2}{3} P_\chi. \quad (20)$$

If b is negative, the satellite migrates toward the planet and positive b means outward migration. We selected disk models with a discernible bump in surface density structure, as summarized in Table 2. In the following, we refer to the cases with $\delta = 0.01$ as Models 1-5, and $\delta = 1$ as Models 1'-5'. The radial distribution of b for Models 1-5 with a satellite of Io mass is given in Figure 6. If a Io-sized satellite that formed at outer radii migrates inward, the migration halts at locations marked with crosses in Fig. 6. Moons migrate all the way to the planet in Model 5 because there is no location where the

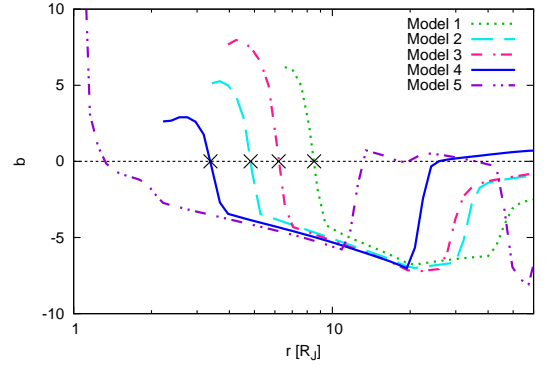


Figure 6. Migration coefficient for an Io-sized moon in the disk model given in Section 2 for Models 1-5. The positions where the migration stops for each model are indicated by crosses.

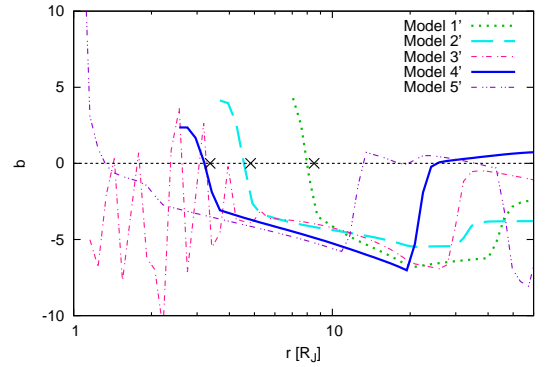


Figure 7. Migration coefficient for an Io-sized moon for Models 1'-5'. For the comparison, the positions where the first moons stop migration for Models 1, 2, and 4 are marked with cross signs.

value of b changes from positive to negative as r increases.

Figure 7 shows plots of b for Models 1'-5' with $\delta = 1$, that is, solar abundance. The location for the termination of moon migration is slightly further inside in Models 1', 2', and 4' compared to Models 1, 2, and 4, respectively, whereas the convergence region disappears in Model 3' as compared to Model 3. If a satellite migrates and stays at $b \simeq 0$, the second satellite migrating from the outer disk approaches the first one that is trapped inside the location of convergent migration. If the migration timescale of the second satellite is longer than the critical time scale, t_m^{crit} , at the location of the first satellite, the second satellite is captured in a mean motion resonance. As mentioned in Ogihara & Kobayashi (2013), the capture probability for higher-order resonances is very low, and moreover the 2:1 MMR is the outermost among first-order resonances – we hence exclusively focus on this case. The critical time scale for capture into 2:1 MMR of equal-mass satellites is given by (Ogihara & Kobayashi 2013)

$$t_m^{\text{crit}} = 2.5 \times 10^4 \left(\frac{M_s}{M_{\text{Io}}} \right)^{-4/3} \left(\frac{M_p}{M_J} \right)^{4/3} T_K, \quad (21)$$

where M_{Io} is the mass of Io and T_K is the orbital period of the satellite. Here, we only consider satellites with equal masses because Galilean satellites have similar masses.

In Model 1, the first satellite is located at about $8.5R_J$ after the termination of migration. A satellite in 2:1 resonance with the satellite at $8.5R_J$ has an orbit at approximately $14R_J$. The corresponding migration timescale is $t_m(14R_J) \simeq 1500\text{yr}$, which is longer than the critical time scale for the first satellite, $t_m^{\text{crit}}(8.5R_J) = 97\text{yr}$. This means that the second satellite is captured in the resonance. Similarly, the third satellite can be captured in the 2:1 resonance of the second satellite at $21R_J$ because $t_m(21R_J) \simeq 2600\text{yr} > t_m^{\text{crit}}(14R_J) \simeq 200\text{yr}$. In this way, we successfully build-up a system in Laplace resonances.

The positions where the first satellite terminate for Models 2-4 are $4.8R_J$, $6.2R_J$, and $3.4R_J$, and the 2:1 resonance orbits of these are $7.6R_J$, $9.8R_J$, and $5.4R_J$, respectively. The orbits in 2:1 resonance with the second satellites are $12R_J$, $16R_J$, and $8.6R_J$, respectively. As summarized in Table 3, the migration timescale of each of these orbits is larger than the critical timescale for capture in the mean motion resonance. Thus, we can also obtain systems in the Laplace resonance with Models 2-4, as well as Model 1. Similarly, we can form those systems in Models 1', 2' and 4'. The comparison of orbits of Models 1-4, 1', 2' and 4' with the Galilean moons are given in Figure 8. Note that the orbits of the resonant three moons are located on the same slope of the surface density profile in all models. One can see that Model 3 has a similar set of orbits with the inner three moons of the Galilean system.

5. DISCUSSION

We summarize the orbits of satellites in our Model 3 along with the mass and orbits of the inner three Galilean moons that are in the Laplace resonance in Table 4. Systems in other models are more compact or spread-out compared with the Galilean moons, but most importantly, the moons are in the 4:2:1 MMR. Once they are in

	Migration timescale		Critical timescale	
Model 1	$t_m(14R_J) = 1500\text{yr}$	$>$	$t_m^{\text{crit}}(8.5R_J) = 97\text{yr}$	
	$t_m(21R_J) = 2600\text{yr}$	$>$	$t_m^{\text{crit}}(14R_J) = 200\text{yr}$	
Model 2	$t_m(7.6R_J) = 5000\text{yr}$	$>$	$t_m^{\text{crit}}(4.8R_J) = 41\text{yr}$	
	$t_m(12R_J) = 7600\text{yr}$	$>$	$t_m^{\text{crit}}(7.6R_J) = 82\text{yr}$	
Model 3	$t_m(9.8R_J) = 760\text{yr}$	$>$	$t_m^{\text{crit}}(6.2R_J) = 60\text{yr}$	
	$t_m(16R_J) = 1300\text{yr}$	$>$	$t_m^{\text{crit}}(9.8R_J) = 120\text{yr}$	
Model 4	$t_m(5.4R_J) = 2500\text{yr}$	$>$	$t_m^{\text{crit}}(3.4R_J) = 24\text{yr}$	
	$t_m(8.6R_J) = 4000\text{yr}$	$>$	$t_m^{\text{crit}}(5.4R_J) = 49\text{yr}$	

Table 3

Comparison between type-I satellite migration timescales, t_m , and critical timescales, t_m^{crit} , for capture into MMR.

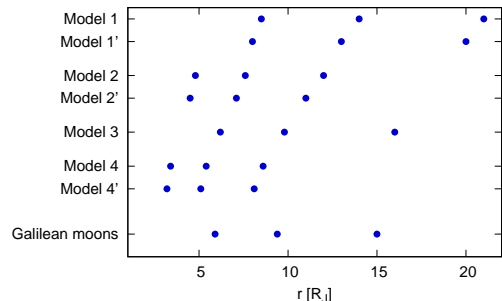


Figure 8. Comparison of the resonant orbits of the satellites obtained in our models with those of the Galilean moons.

	Galilean Moons		Model 3
	Mass (10^{25} g)	Orbit (R_J)	Orbit (R_J)
Io	8.93	5.9	6.2
Europa	4.80	9.4	9.8
Ganymede	14.8	15.0	16

Table 4

Summary of satellite properties

this resonance, the orbits are locked and the moons migrate together as a system; the separations of the bodies adjust accordingly, when the whole system moves radially during the evolution of the CPD.

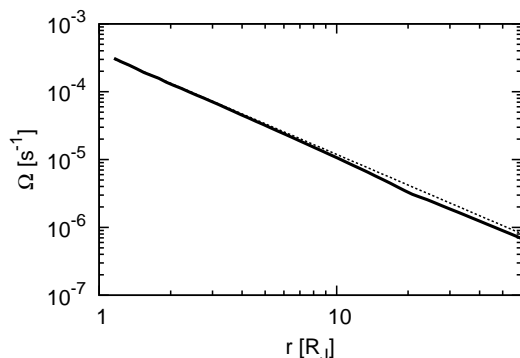


Figure 9. Angular velocity of the disk for Model 4. Keplerian frequency is also plotted in the dotted line.

Figures 4 and 5 show that the disk is quite hot at this stage. At such high disk temperatures, the radial pressure gradient may lead to sub-Keplerian rotation velocities. Actually, as Fig. 9 shows, the angular velocity is smaller than the Keplerian value in the

outer part of the disk. The angular velocity is calculated as $\Omega = \Omega_K(1 - \eta)^{1/2}$, where $\eta = -(r\Omega_K^2\rho)^{-1}\partial P/\partial r$ (Takeuchi & Lin 2002). We assumed Keplerian rotation profiles when we derived disk models. However, since Equation (1) is only sensitive to the radial *slope* of the angular velocity, the assumption is expected to be acceptable.

Hot CPDs are suggested by Keith & Wardle (2014), Zhu (2015), and Szulágyi et al. (2016), but it may be difficult to form icy satellites in such an environment. Since the outer disk is cooler, moons may gain icy materials simply by migrating in from larger radii. Although Fig. 6 shows b is positive in $r \gtrsim 25R_J$ for Model 4, for instance, bodies about ten times smaller than Io can migrate all the way from the outer radii because b for them remains negative at all radii. Another possibility is that ice-rich planetesimals are captured when they enter into the CPD. Tanigawa et al. (2014) found that the orbits of sub-Io sized planetesimals captured in a CPD are highly eccentric. They also found that 10 m or larger planetesimals can be efficiently captured in a CPD, thus those bodies may grow into the size of present moons.

One problem is, however, whether the system can survive over the long-term evolution of the CPD. As mass infall decreases, the temperature of the disk also decreases. When the disk structure that traps the innermost body disappears, the satellite system will start to migrate toward the planet. Moons can survive if the CPD is quickly cleared before they are lost into the planet. A rough estimate of the viscous timescale of the disk is $r^2/\nu \sim 100$ yr, which is shorter than the migration timescale of the satellites. However, the actual timescale for the surface density to become small enough not to affect satellite migration is most likely to be much longer than this estimate. Clearly, this depends on how the disk dissipates and many other unknown factors. In order to obtain a better understanding of how the infall terminates, we need to further study the evolution of PPDs including both gap formation and gas dissipation. In this work, we adopted a mass infall rate derived from isothermal hydrodynamic simulations, however, Gressel et al. (2013) suggested that taking magnetic field and radiative cooling into account leads to a different mass infall rate, which opens a perspective for future work.

Sasaki et al. (2010) and Ogihara & Ida (2012) found that the existence of an inner cavity in a CPD can prevent a moon system from being lost onto the planet. Provided the planet rotates differentially (given that it accretes material with non-negligible angular momentum this is not unreasonable to assume) and maintains a convective or turbulent sub-surface flow, it can be expected to harbor an efficient planetary dynamo. In this case, such an inner cavity may form due to magnetospheric truncation of the sub-disk by the planet’s dipole magnetic field. In the context of PPDs, not only photoevaporative but also magnetically driven disk wind have been reported to contribute to the formation of so-called “transition disks” (Suzuki et al. 2010) with reduced surface density at small radii. To explore such currently unknown effects in the context of embedded sub-disks, the configuration of magnetic field at the very vicinity of the planet must be studied.

We have modeled massive and comparatively hot CPDs by solving the time evolution of surface density with mass infall from the parental PPD. The mass infall flux was determined based on the high-resolution numerical simulation of Tanigawa et al. (2012), where we have also considered the reduction of the flux caused by the dissipation of the PPD at the location of the sub-disk. The temperature profile of the CPD is derived by the balance of viscous heating and radiative cooling, as well as the radial advection. Since the strength of viscosity is uncertain in the absence of MRI, we employed a parameter to determine the minimum value of the viscosity. We considered the MRI when the Elsasser number exceeds unity due to thermal ionization. We furthermore monitored Toomre’s Q parameter in order to consider effective viscosity when the value becomes lower than about two. When the evolution is governed by α_{floor} , the system settles into a steady state.

In many previous studies, the critical temperature for the onset of the MRI is assumed to be at about 1000 K. As shown in Figure 1, however, we found that this is not the case for massive CPDs. This is because of the two reasons: (i) the ionization degree needed to sustain the MRI in a CPD is higher than that in a PPD, and (ii) thermal ionization is less effective in higher density regions. In our models, MRI is turned on by thermal ionization only around $T \sim 2000 - 3000$ K.

We found that opacity transitions change the radial dependence of the temperature structure, and especially, a transition near 2000 K makes a bump in surface density distribution. We estimated whether a moon migrating toward the central planet can be trapped at such a location. In the case of some of the parameter settings that are referred to as Models 1-4, 1’, 2’, and 4’, the surface-density and temperature gradients were sufficiently steep to stop the migration of a moon. Moreover, we have examined the migration timescales of the second and third moons migrating inward and compared them to the critical timescale to be captured in a 2:1 MMR with the inner moon. In all of Models 1-4, 1’, 2’, and 4’, we obtained systems in 4:2:1 mean motion resonance that is known for inner three bodies of the Galilean system. The satellite system obtained in our disk models may or may not survive until the dissipation of the CPD. In order to find out the long term evolution of these systems, further studies on mass infall from PPDs and on the origin of angular momentum transport in CPDs are needed.

We thank the anonymous referee for a careful report. We acknowledge Shigeo S. Kimura, Pablo Benítez-Llambay, Shigeru Ida, Masahiro Ogihara, and Kazuhiro D. Kanagawa for fruitful discussions and Edwin L. Turner for encouraging comments. HK was supported by Grants-in-Aid for Scientific Research (No. 26287101) from Ministry of Education, Culture, Sports, Science and Technology (MEXT) of Japan and by Astrobiology Center Project of the National Institute of Natural Science (NINS) (Grant Number AB281018). OG has received funding from the European Research Council (ERC) under the European Union’s Horizon 2020 research and innovation programme (grant agreement No 638596).

- Armitage, P. J., Livio, M., & Pringle, J. E. 2001, *MNRAS*, 324, 705
- Ayliffe, B. A., & Bate, M. R. 2009, *MNRAS*, 393, 49
- Balbus, S. A., & Hawley, J. F. 1991, *ApJ*, 376, 214
- Bell, K. R., & Lin, D. N. C. 1994, *ApJ*, 427, 987
- Blaes, O. M., & Balbus, S. A. 1994, *ApJ*, 421, 163
- Cannizzo, J. K. 1993, *ApJ*, 419, 318
- Canup, R. M., & Ward, W. R. 2002, *AJ*, 124, 3404
- . 2006, *Nature*, 441, 834
- Charnoz, S., Salmon, J., & Crida, A. 2010, *Nature*, 465, 752
- Crida, A., & Charnoz, S. 2012, *Science*, 338, 1196
- Estrada, P. R., & Mosqueira, I. 2006, *Icarus*, 181, 486
- Fujii, Y. I., Okuzumi, S., & Inutsuka, S. 2011, *ApJ*, 743, 53
- Fujii, Y. I., Okuzumi, S., Tanigawa, T., & Inutsuka, S. 2014, *ApJ*, 785, 101
- Gressel, O., Nelson, R. P., Turner, N. J., & Ziegler, U. 2013, *ApJ*, 779, 59
- Hayashi, C. 1981, *Progress of Theoretical Physics Supplement*, 70, 35
- Hyodo, R., Charnoz, S., Genda, H., & Ohtsuki, K. 2016, *ApJ*, 828, L8
- Hyodo, R., Charnoz, S., Ohtsuki, K., & Genda, H. 2017, *Icarus*, 282, 195
- Hyodo, R., Ohtsuki, K., & Takeda, T. 2015, *ApJ*, 799, 40
- Keith, S. L., & Wardle, M. 2014, *MNRAS*, 440, 89
- Kimura, S. S., & Tsuribe, T. 2012, *PASJ*, 64, 116
- Klahr, H., & Kley, W. 2006, *A&A*, 445, 747
- Kretke, K. A., & Lin, D. N. C. 2012, *ApJ*, 755, 74
- Lin, M.-K., & Youdin, A. N. 2015, *ApJ*, 811, 17
- Lubow, S. H., & Martin, R. G. 2012, *ApJ*, 749, L37
- . 2013, *MNRAS*, 428, 2668
- Lunine, J. I., & Stevenson, D. J. 1982, *Icarus*, 52, 14
- Machida, M. N., Kokubo, E., Inutsuka, S., & Matsumoto, T. 2010, *MNRAS*, 405, 1227
- Martin, R. G., & Lubow, S. H. 2011, *ApJ*, 740, L6
- . 2013, *MNRAS*, 432, 1616
- Mosqueira, I., & Estrada, P. R. 2003a, *Icarus*, 163, 198
- . 2003b, *Icarus*, 163, 232
- Nelson, R. P., Gressel, O., & Umurhan, O. M. 2013, *MNRAS*, 435, 2610
- Ogihara, M., & Ida, S. 2012, *ApJ*, 753, 60
- Ogihara, M., & Kobayashi, H. 2013, *ApJ*, 775, 34
- Ogihara, M., Kobayashi, H., Inutsuka, S.-i., & Suzuki, T. K. 2015, *A&A*, 579, A65
- Okuzumi, S., & Hirose, S. 2011, *ApJ*, 742, 65
- Okuzumi, S., & Ormel, C. W. 2013, *ApJ*, 771, 43
- Paardekooper, S.-J., Baruteau, C., & Kley, W. 2011, *MNRAS*, 410, 293
- Perez, S., Dunhill, A., Casassus, S., et al. 2015, *ApJ*, 811, L5
- Rivier, G., Crida, A., Morbidelli, A., & Brouet, Y. 2012, *A&A*, 548, A116
- Sano, T., & Miyama, S. M. 1999, *ApJ*, 515, 776
- Sasaki, T., Stewart, G. R., & Ida, S. 2010, *ApJ*, 714, 1052
- Shakura, N. I., & Sunyaev, R. A. 1973, *A&A*, 24, 337
- Suzuki, T. K., Muto, T., & Inutsuka, S.-i. 2010, *ApJ*, 718, 1289
- Szulágyi, J., Masset, F., Lega, E., et al. 2016a, *MNRAS*, 460, 2853
- Szulágyi, J., Mayer, L., & Quinn, T. 2017, *MNRAS*, 464, 3158
- Szulágyi, J., Morbidelli, A., Crida, A., & Masset, F. 2014, *ApJ*, 782, 65
- Takahashi, S. Z., Inutsuka, S.-i., & Machida, M. N. 2013, *ApJ*, 770, 71
- Takeuchi, T., & Lin, D. N. C. 2002, *ApJ*, 581, 1344
- Tanigawa, T., Maruta, A., & Machida, M. N. 2014, *ApJ*, 784, 109
- Tanigawa, T., Ohtsuki, K., & Machida, M. N. 2012, *ApJ*, 747, 47
- Tanigawa, T., & Watanabe, S.-i. 2002, *ApJ*, 580, 506
- Turner, N. J., Lee, M. H., & Sano, T. 2014, *ApJ*, 783, 14
- Zhu, Z. 2015, *ApJ*, 799, 16
- Zhu, Z., Hartmann, L., & Gammie, C. 2010, *ApJ*, 713, 1143